Phase separation kinetics of two-temperature induced phase transition at low density: Cluster growth by ballistic agglomeration

Nayana Venkatareddy [1,*] Partha Sarathi Mondal [2,*] Shradha Mishra [2,†] and Prabal K. Maiti [1,‡]
[1]*Department of Physics, Indian Institute of Science, C. V. Raman Avenue, Bengaluru, Karnataka 560012, India*
[2]*Department of Physics, Indian Institute of Technology (BHU), Varanasi, Uttar Pradesh 221005, India*

(Received 22 December 2025; accepted 22 July 2026; published 3 September 2026)

We study the kinetics of two-temperature induced phase separation in dilute binary mixtures of active ("hot") and passive ("cold") particles using molecular dynamics simulations and a coarse-grained hydrodynamic model. Following a temperature quench, cold particles nucleate into mobile clusters that move ballistically and merge through successive coalescence events. The resulting domain growth exhibits dynamic scaling with a growth exponent ≈0.7, markedly faster than diffusive coarsening. We identify this regime as ballistic agglomeration of cold clusters, demonstrating a distinct nonequilibrium growth mechanism in low-density scalar active systems.

DOI: 10.1103/mpmp-23l4

I. INTRODUCTION

The study of phase separation kinetics constitutes a central theme in condensed-matter physics, elucidating universal features such as scaling behavior, domain growth, and morphological self-similarity during coarsening [1–4]. Beyond the theoretical importance, understanding the kinetics is important for many practical applications, for instance, in the formation of microstructures during the manufacturing of materials [5]. In recent years, with the advances in active matter systems [6–9], the importance of kinetic processes has garnered new interest in the context of far from equilibrium systems showing motility-induced phase separation (MIPS) [10], swarming and flocking [8,11], and active turbulence [12].

In conventional active matter systems, the activity emerges through internal force generation mechanisms of individual agents. In contrast to these systems, in a binary mixture, activity can manifest through effective temperature difference resulting from the difference in the dynamical characteristics of the constituent species - referred to as hot and cold [13,14]. When the temperature difference exceeds a density-dependent critical value, the hot and cold particles phase separate, and is termed two-temperature induced phase separation (2-TIPS). The two-temperature framework has been effectively applied to diverse biological systems like chromosomal dynamics [15], behavior of molecular motors [16], enzymes [17], and cell motility–driven demixing [18]. Additionally, the 2-TIPS framework can serve as a minimal model for tracer dynamics in nonequilibrium media [19].

Due to the versatility of the two-temperature framework, 2-TIPS phenomena have been studied extensively [14,20–27], wherein the cold particles spontaneously assemble into dense clusters exhibiting crystalline order in Lennard-Jones (LJ) monomers and liquid-crystalline (LC) order in spherocylinders. Despite substantial progress in understanding the steady-state behavior, the kinetics of 2-TIPS has remained comparatively unexplored. Recently, we demonstrated that for LJ monomers, the domain growth during 2-TIPS follows a $\sim t^{1/3}$ scaling, both in two and three dimensions, in the high-density regime [28], reminiscent of the Lifshitz-Slyozov (LS) growth law in equilibrium binary mixtures (EBMs) [29]. In EBMs, both the mechanism and kinetics of phase separation are known to depend sensitively on density [2,30], a feature also observed in active systems [31,32]. It is natural to ask whether two-temperature systems display a similar behavior.

In this article, we study the kinetics of 2-TIPS in a low-density binary mixture of hot and cold LJ particles using molecular dynamics (MD) simulations and a corresponding coarse-grained model (CG) coupled to hydrodynamic flow in two dimensions. First, we present the simulation details and results obtained from MD simulations in Sec. II. Next, we describe the CG model and its corresponding results in Sec. III. We find that phase separation begins with the nucleation of cold clusters, which subsequently move ballistically and grow via coalescence, resulting in significantly faster domain growth. The growth exponent obtained from MD simulations is in good agreement with the predictions of ballistic aggregation theory and the results obtained from the CG model. Finally, we conclude our results in Sec. IV.

II. MOLECULAR DYNAMICS SIMULATIONS

A. Simulation details

We investigate the phase separation kinetics of 2-TIPS in a binary mixture of hot and cold particles using molecular dynamics (MD) simulations in two dimensions at low density. The system consists of $N = 80\,000$ particles, equally divided between hot and cold species, confined within a two-dimensional periodic simulation box. All the particles interact

*These authors contributed equally to this work.
†Contact author: smishra.phy@itbhu.ac.in
‡Contact author: maiti@iisc.ac.in

with each other through the Lennard-Jones (LJ) potential described below,

$$U_{\mathrm{LJ}}(r) = 4\epsilon\left[\left(\frac{\sigma}{r}\right)^{12} - \left(\frac{\sigma}{r}\right)^{6}\right], \tag{1}$$

where ϵ denotes the strength of the interaction, σ is the diameter of the LJ particle, and r is the distance between the interacting particles. The results reported here are presented in reduced units, where the length and energy are expressed in units of σ and ϵ, respectively. The use of reduced units is motivated by the law of corresponding states, which asserts that systems described by the same reduced variables exhibit similar thermodynamic behavior. Accordingly, the density and temperature in reduced units are given by $\rho^* = \rho\sigma^2$ and $T^* = k_{\mathrm{B}}T/\epsilon$, respectively.

The simulations were performed in the *NVT* ensemble using the LAMMPS [33] software. To introduce the two-temperature model, we assign half of the particles in the system to the cold thermostat and the remaining half to the hot thermostat. We use the Nosé-Hoover thermostat [34] to maintain the temperature of both hot (T_{h}^*) and cold (T_{c}^*) particles. The time step of integration is $\Delta t^* = 0.0005$, and the damping factor of the thermostat is chosen as $\tau_{\mathrm{T}} = 50 \times \Delta t^*$ as used in our previous works [14,22]. All the simulations in the present work are carried out at a low density of $\rho^* = 0.1$.

Our previous studies have demonstrated [14,22] that hot and cold particles undergo macroscopic phase separation when the temperature of hot particles is equal to or exceeds $T_{\mathrm{h}}^* = 25$ at the density of $\rho^* = 0.1$. To investigate the kinetics of 2-TIPS, we first prepare the binary mixture in a homogeneous state by setting the temperatures of both hot (T_{h}^*) and cold (T_{c}^*) particles to $T^* = 2$. The system is equilibrated under these conditions for 4 million (M) time steps to ensure complete mixing. Subsequently, the system is quenched from this mixed state to a phase-separated state by instantaneously increasing the temperature of the hot particles to $T_{\mathrm{h}}^* = 25$. We also perform an additional quench at $T_{\mathrm{h}}^* = 40$. Following each quench, the simulations are carried out for 10M time steps, during which we analyze and quantify the temporal evolution of the domain morphologies as the system evolves from a homogeneous state to a phase-separated nonequilibrium steady state. All the dynamic quantities presented here are averaged over 10 independent runs to ensure a good statistical estimate.

B. Results

1. Kinetics of phase separation

The instantaneous snapshots of the phase separating binary mixture at different instants of time, for quench temperature $T_{\mathrm{h}}^* = 25$ at density $\rho^* = 0.1$, are given in Figs. 1(a)–1(c). During the early stages, postquench, small, isolated nuclei of cold particles emerge within a sea of hot particles. These cold clusters initially maintain a nearly circular shape during their growth prior to reaching 1M time steps. Subsequently, these isolated cold clusters coalesce with each other to form larger elongated clusters, ultimately leading to phase separation. The cold clusters exhibit high-density crystalline order with the constituent particles arranged in a hexagonal lattice, as shown in Fig. 1(d), as they are compressed and stabilized by the kinetic pressure of the hot particles. The coexistence of dense

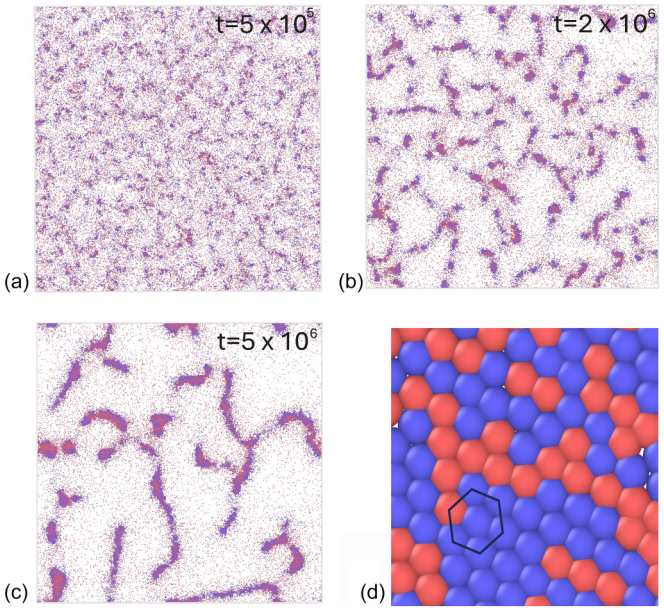

FIG. 1. Panels (a), (b), and (c) illustrate the instantaneous snapshots of phase separating hot (red) and cold (blue) particles at density $\rho^* = 0.1$ and quench temperature $T_{\mathrm{h}}^* = 25$, at different instants of time. Initially ($t = 5 \times 10^5$), small circular cold nuclei form, which later coalesce into larger, elongated clusters ($t = 2 \times 10^6, 5 \times 10^6$). (d) Magnified view of a cold cluster showing hexagonal ordering of cold particles and trapping of hot particles within the cluster.

cold domains with a dilute hot phase is a hallmark feature of systems undergoing 2-TIPS and is consistently observed across a broad class of soft matter systems [14,20,22,23]. Due to their crystalline order, cold clusters behave distinctly from liquid droplets undergoing phase separation [1,35,36]. While liquid droplets typically maintain circular shapes due to dominant surface tension effects, the cold clusters here tend to form elongated or fractal morphologies due to the slower reorientation dynamics [37] of solidlike structures. We also note the enhanced trapping of hot particles in the phase separating cold clusters (Fig. 1), particularly at the late stages. This characteristic of 2-TIPS at low dimensions ($d < 3$) [22] is mainly due to the reduction of the cold-hot interface with decreasing dimension, thereby decreasing the number of pathways for hot particles to escape from the dense cold cluster. This mechanism of cluster coalescence is different from the phase separation kinetics of 2-TIPS at high density [28], where bicontinuous domains rich in either hot or cold particle grow progressively with time, akin to spinodal decomposition in passive systems.

2. Correlation function and growth law

To quantify the domain morphologies of the phase separating binary mixture, we first establish an order parameter field $\phi(r, t)$ which can effectively distinguish the hot and cold domains. Since the phase separating cold particles form denser regions compared to the hot particles, we use the local density differences between these regions to differentiate the two domains. Following the same procedure as in our previous work [28], we define a local density field $\rho(r, t)$ by mapping

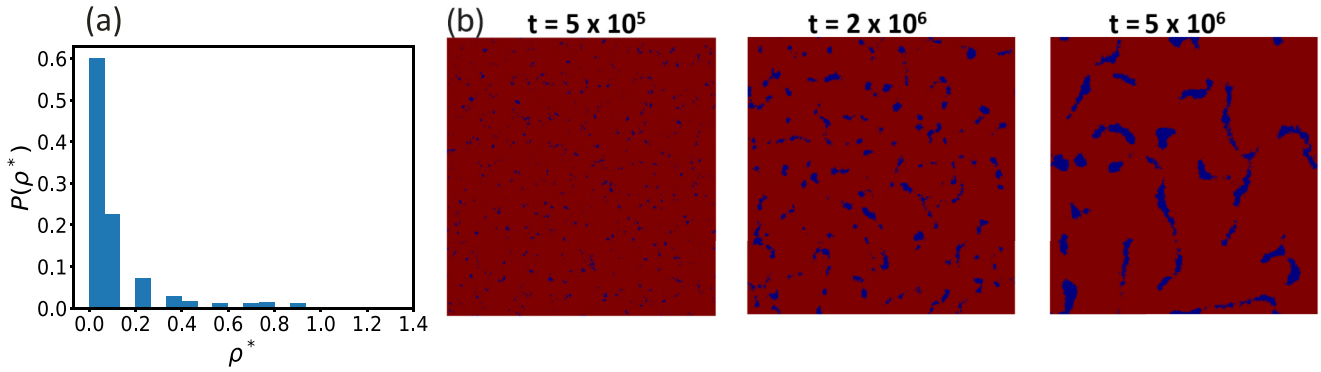

FIG. 2. (a) The plot depicts the histogram representing the probability distribution $P(\rho^*)$ of the local density ρ^* of the phase separating binary mixture, at low overall density $\rho^* = 0.1$ and $T_h^* = 25$, at time $t = 2 \times 10^6$. The distribution clearly shows that the dilute hot particles occupy a larger fraction of the simulation area, while the dense colder domains are confined to comparatively smaller area. (b) The figure shows order parameter field $\phi(r, t)$ for quench temperature $T_h^* = 25$ and density $\rho^* = 0.1$, at various instants of time. The cold particle-rich regions with high density $[\rho^*(r) > 0.5]$ are assigned $\phi(r) = 1$ and are depicted in dark blue, while hot particle-rich regions with low density $[\rho^*(r) <= 0.5]$ are assigned $\phi(r) = -1$ and are represented by dark red.

the particle positions in the simulation domain onto a lattice with spacing σ (the diameter of a LJ particle). The local density at each lattice site is then computed by counting the number of nearest neighbors.

Figure 2(a) depicts the histogram of local density distribution $P(\rho^*)$ at time $t = 2 \times 10^6$ for the global density of $\rho^* = 0.1$ and $T_h^* = 25$. The probability decreases with increasing local density and becomes nearly constant for $\rho^* \geqslant 0.4$. This distribution indicates that the simulation domain is predominantly occupied by dilute hot particles, while the dense cold domains occupy a smaller fraction of the area. Given the crystalline structural arrangement of cold domains, lattice sites with a majority of occupied neighboring sites (five or more out of nine) are classified as cold regions, and the rest as hot regions. Consequently, from the local density field $\rho(r, t)$, the hardened order parameter field $\phi(r, t)$ is obtained by assigning $\phi = 1$ to dense cold regions $[\rho(r) > 0.5]$ and $\phi = -1$ to dilute hot regions $[\rho(r) <= 0.5]$. The order parameter field $\phi(r, t)$ for quench temperature $T_h^* = 25$ and density $\rho^* = 0.1$, at various instants of time, is illustrated in Fig. 2(b). The order parameter field clearly differentiates the cold clusters (blue) from the surrounding dilute hot regions (red).

To obtain the average length of the cold domains, we calculate the two-point spatial correlation function of the order parameter field as defined below,

$$C_\phi(r, t) = \langle \phi(\boldsymbol{r}_0, t)\phi(\boldsymbol{r}_0 + \boldsymbol{r}, t)\rangle - \langle \phi(\boldsymbol{r}_0, t)\rangle\langle \phi(\boldsymbol{r}_0 + \boldsymbol{r}, t)\rangle, \tag{2}$$

where $\langle \cdots \rangle$ denotes averaging over directions of $\boldsymbol{r}$ for a fixed $r = |\boldsymbol{r}|$, the reference point $\boldsymbol{r}_0$ as well as multiple independent realizations. The characteristic length $l(t)$, a measure of the domain size, is defined as the distance at which $C_\phi(r, t)$ decays to half (0.5) of its value at $r = 0$. The insets of Figs. 3(a) and 3(b) present the plots of correlation function $C_\phi(r, t)$ versus distance r for $T_h^* = 25$ and 40, respectively, at different instants of time following the quench. We observe that decay of $C_\phi(r, t)$ with r becomes slower over time, implying that the size of phase separating domains increases as time progresses. After 1M time steps postquench, the phase separation kinetics enters a scaling regime. When plotted against the rescaled distance $r/l(t)$, $C_\phi(r, t)$ at different times collapse onto a single master curve as shown in Figs. 3(a) and 3(b), indicating that the domain morphologies are statistically self-similar and differ solely in their characteristic length scale $l(t)$. In Figs. 3(c) and 3(d), we present the plots of $l(t)$ versus time t for $T_h^* = 25$ and 40, respectively. At late times, we see that $l(t)$ grows algebraically with time, typical of domain growth in kinetics, given by $l(t) \sim t^{1/z}$, where $1/z$ is the growth exponent. Our calculations show that the value of the growth exponent at late times is $1/z = 0.71 \pm 0.03$ and 0.68 ± 0.04 for $T_h^* = 25$ and 40, respectively. Additional simulations with $N = 100\,000$ particles and quench temperature $T_h^* = 25$, presented in Appendix A, also yield a high growth exponent of $1/z = 0.67 \pm 0.03$, demonstrating the robustness of the exponent with respect to system size. The growth exponent of 2-TIPS at low density, for both quench temperatures studied here, is significantly larger than the LS exponent of 1/3 observed at high density [28].

3. Cluster motion prior to coalescence

To investigate the origin of faster growth, we further analyze the coalescence mechanism by performing cluster analysis using the DBSCAN [38] algorithm. Two particles are assigned to the same cluster if their separation is less than a cutoff distance r_c. The value of $r_c = 1.2\sigma$ is obtained from the first peak of the radial distribution function of cold particles in the phase separated steady state, evaluated from our previous studies [14,22]. After identifying the cold clusters, we analyze the dynamics of the clusters prior to coalescence. However, the size of many of these cold clusters shows large fluctuations with time. So, we carefully select 20 clusters that do not show large fluctuations in size during the time of their observations. We calculate the mean-square displacement (MSD) $\Delta(t)$ of the center of mass (cm) of the selected clusters as $\Delta(t) = \langle [\boldsymbol{r}_{\rm cm}(t) - \boldsymbol{r}_{\rm cm}(0)]^2 \rangle \sim t^\gamma$, where $\boldsymbol{r}_{\rm cm}$ is the position of cm of the cluster, and γ denotes the scaling exponent associated with MSD. Figures 4(a) and 4(b) show log-log plots of $\Delta(t)$ versus t, from which the value of the exponent $\gamma \approx 2.1$ and 1.9, for

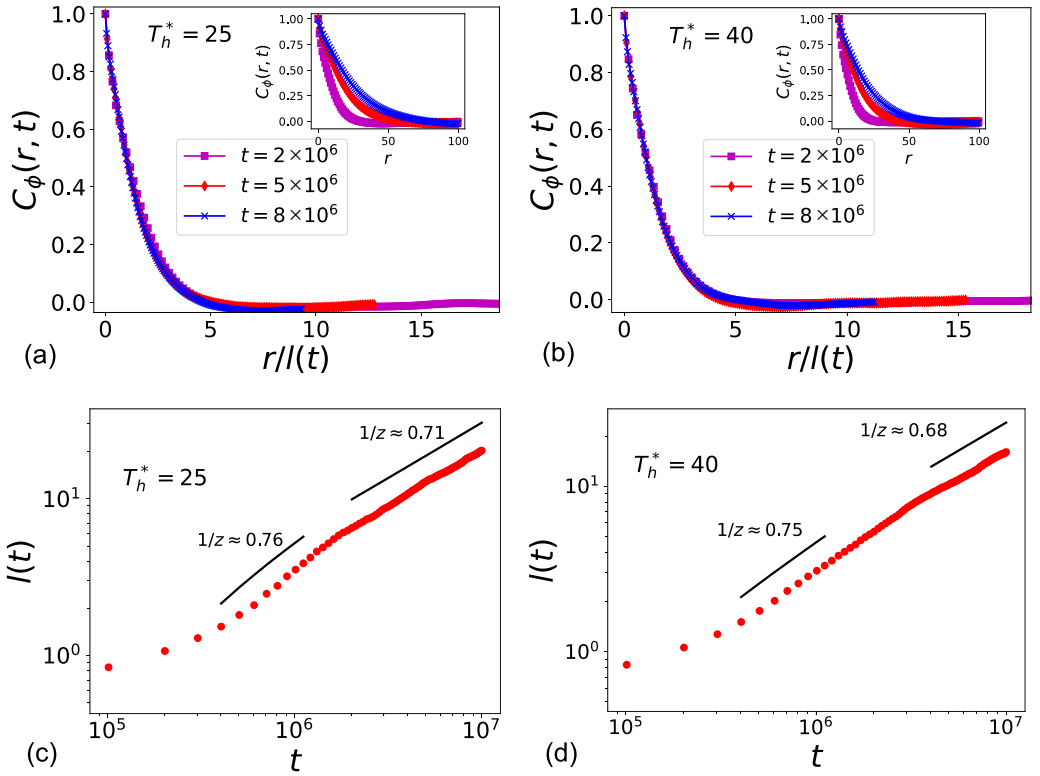

FIG. 3. (a) and (b) Plots of the two-point spatial correlation function of ϕ, $C_\phi(r,t)$ as a function of rescaled distance $r/l(t)$, at density $\rho^* = 0.1$, for $T_h^* = 25$ and 40, respectively, at different instants of time. The $C_\phi(r,t)$ at different times collapses onto a single master plot demonstrating dynamic scaling. Insets illustrate the corresponding plots of two-point spatial correlation function of ϕ, $C_\phi(r,t)$ as a function of distance between the points r, at different instants of time. (c) and (d) Log-log plots of characteristic length $l(t)$ vs time t for $T_h^* = 25$ and 40, respectively, show algebraic growth of $l(t)$. The value of growth exponent $1/z$ at late times is equal to 0.71 ± 0.03 and 0.68 ± 0.04 for $T_h^* = 25$ and 40, respectively.

$T_h^* = 25$ and 40, respectively, is obtained. This indicates that the clusters exhibit ballistic motion preceding collision. The ballistic motion of cold clusters is counterintuitive, as one would anticipate a cold cluster immersed in a sea of hot particles to exhibit diffusive motion. However, a visual inspection of the cluster agglomeration process reveals that the isolated clusters move towards each other as if there is an effective attractive force between them. This may originate from the nonuniform forces exerted by the hot particles on the cold clusters, likely a consequence of the uneven instantaneous temperatures of hot particles, which vary with proximity to the cold clusters (hot particles in the immediate vicinity of cold clusters have lower temperatures due to increased heat transfer to the cold particles). Consequently, the motion of cold clusters is primarily ballistic rather than diffusive. In Movies 1 and 2 [50], we show the dynamics of a few clusters, which clearly show the ballistic motion.

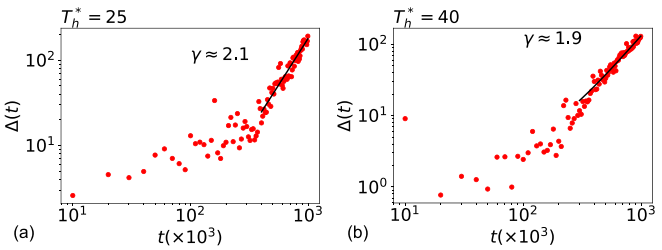

FIG. 4. Panels (a) and (b) depict the MSD $\Delta(t)$ of cold clusters with time t on a log-log scale for $T_h^* = 25$ and 40, respectively. The black curve represents the power-law dependence of MSD on time $\Delta(t) \sim t^\gamma$, with exponent $\gamma \approx 2$, implying the ballistic nature of cluster motion.

4. Theoretical prediction of growth exponent

The cluster growth dynamics of ballistically moving clusters can be theoretically [37,39–41] analyzed as follows. Consider a system in d-dimensional space with N clusters moving ballistically with a root-mean-square (rms) velocity v. Let n be the number density of clusters and m be the average mass of clusters at a given time t. Assuming the clusters to be nonspherical in shape, the size of the clusters is characterized by their radius of gyration R_g, also a measure of collision cross section. The average mass of clusters m evolves with time as given in the equation below,

$$\frac{dm}{dt} = \frac{m}{\tau}, \tag{3}$$

where $\tau = \frac{1}{nvR_g^{d-1}}$ (ratio of average volume per cluster to the rate of volume swept by the cluster) is the average time of collision between two clusters. We rewrite n, v, and R_g in terms of average mass m as $n \sim m^{-1}$, $v \sim m^{-z'}$, and $m \sim R_g^{d_f}$, respectively. Here z' and fractal dimension d_f are the exponents associated with mass dependence on velocity v

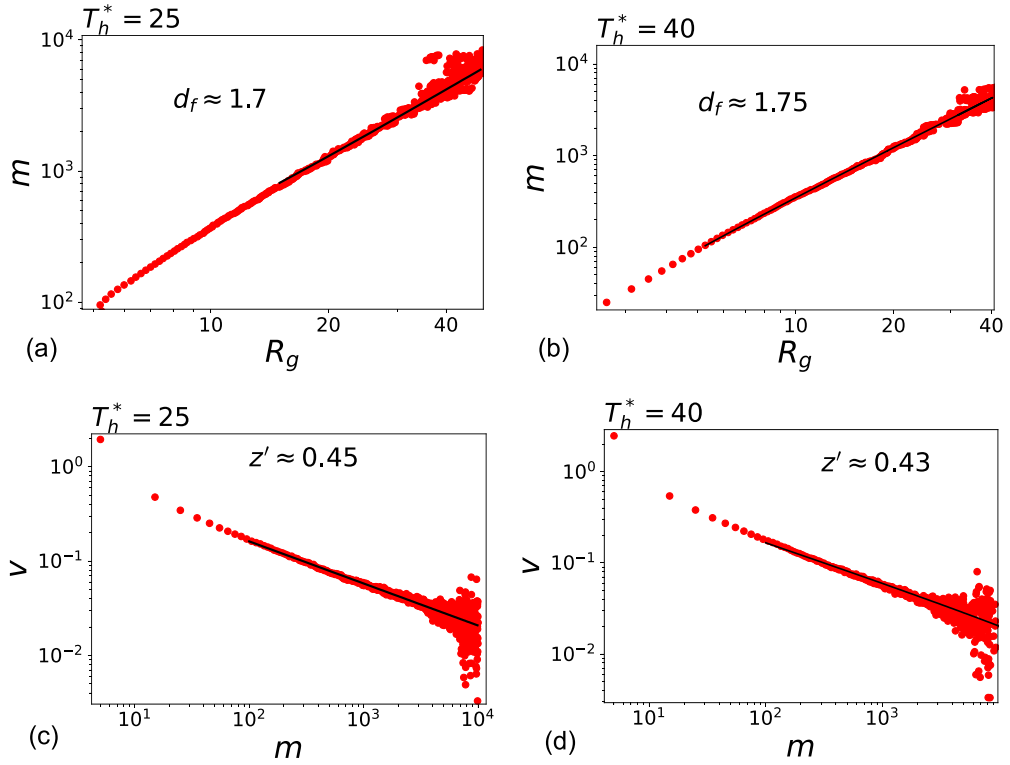

FIG. 5. (a) and (b) Log-log plots of average mass of clusters m vs average radius of gyration R_g for $T_h^* = 25$ and 40, respectively. The power-law exponent ($m \sim R_g^{d_f}$) associated with it is $d_f \approx 1.7$ and 1.75 for $T_h^* = 25$ and 40, respectively. (c) and (d) Log-log plots of average rms velocity of clusters v vs average mass m for $T_h^* = 25$ and 40, respectively. The associated power-law decay exponent ($v \sim m^{-z'}$) is $z' \approx 0.45$ and 0.43 for $T_h^* = 25$ and 40, respectively.

and radius of gyration R_g, respectively. Substituting them in Eq. (3), we obtain the solution

$$m \sim t^{\beta}, \beta = \frac{d_f}{d_f(1+z') - (d-1)}. \tag{4}$$

To obtain the theoretical mass growth exponent, β_{theory}, for low-density kinetics in 2-TIPS, we evaluate the fractal dimension d_f and the velocity-mass scaling exponent z' for the phase separating cold clusters. Using cluster analysis, we monitor the time evolution of the cluster mass m, radius of gyration R_g, and the rms center-of-mass velocity v.

Figures 5(a) and 5(b) and Figs. 5(c) and 5(d) present the scaling of the average radius of gyration R_g and average rms velocity v with average cluster mass m, respectively. From Figs. 5(a) and 5(b), we extract the fractal dimension of the cold clusters as $d_f \approx 1.7$ for $T_h^* = 25$ and $d_f \approx 1.75$ for $T_h^* = 40$. Since $d_f < d = 2$, this confirms that the cold clusters deviate from circular morphology, consistent with our earlier observations. From Figs. 5(c) and 5(d), we obtain the velocity scaling exponent $z' \approx 0.45$ for $T_h^* = 25$ and $z' \approx 0.43$ for $T_h^* = 40$.

Using these measured exponents, we compute $\beta_{\text{theory}} \approx 1.16$ for $T_h^* = 25$, which yields a theoretical domain growth exponent $1/z_{\text{theory}} = \beta_{\text{theory}}/d_f \approx 0.68$. This value is in good agreement with the growth exponent $1/z \approx 0.71$ obtained from the domain length plot [Fig. 3(c)], calculated from the decay of the correlation function $C_\phi(r,t)$. Similarly, for $T_h^* = 40$, we obtain $\beta_{\text{theory}} \approx 1.17$ and $1/z_{\text{theory}} \approx 0.66$, which closely agrees with the measured value $1/z \approx 0.68$ from the spatial correlation of the order parameter field [Fig. 3(d)]. The consistency between the theoretically predicted and independently measured growth exponents establishes cluster coalescence via ballistic agglomeration as the dominant mechanism governing 2-TIPS kinetics in the low-density regime. Further, the plot of the average mass of 20 largest clusters $\langle m \rangle$ versus time t, presented in Appendix B, gives $\beta \approx 1.2$ and 1.24 for $T_h^* = 25$ and 40, respectively, consistent with their theoretical values β_{theory}.

III. COARSE-GRAINED SIMULATIONS

A. Model and simulation details

We propose a coarse-grained (CG) model to provide an effective mesoscopic description of the system. At the microscopic level, particle dynamics in a medium are governed by interparticle interactions as well as inertia, and the state of the system is specified by the positions and momenta of all particles. In contrast, at the mesoscopic scale, the dynamics are described in terms of the time evolution of slow variables, whose selection is dictated by the underlying symmetries and conservation laws. Since the total number of particles is conserved, the local density field, $\rho(\boldsymbol{r})$, naturally emerges as a slow variable. In addition, in systems where momentum is conserved or relaxes over time scales much longer than microscopic ones (e.g., in low-viscosity fluids), the momentum density, $\boldsymbol{g}(\boldsymbol{r})$, also acts as a slow variable. The

corresponding velocity field, $\boldsymbol{u}(\boldsymbol{r}) = \boldsymbol{g}/\rho$, then evolves according to the Navier-Stokes equation (NSE). Thus, the system is described by a set of coupled equations involving the conserved order-parameter fields corresponding to the densities of the cold and hot species, $\psi_{\rm c}(\boldsymbol{r})$ and $\psi_{\rm h}(\boldsymbol{r})$, along with the velocity field $\boldsymbol{u}(\boldsymbol{r})$, which captures the local flow and momentum transport due to both hot and cold species in the system.

The dynamics of the $\psi_{\rm c}(\boldsymbol{r})$ and $\psi_{\rm h}(\boldsymbol{r})$ fields are, to leading order, governed by an effective free-energy functional. At the mesoscopic scale, the coupling between the hot and cold species arises from the coarse-grained contribution of binary interspecies interactions to their effective dynamics.

The presence of clusters of cold particles in the sea of hot particles creates temperature gradients at the surface of the cluster; the temperature is low inside and increases gradually across the interface. This temperature gradient generates an effective drive due to the local density difference of cold and hot particles across the interface. This also leads to the enhanced velocity with finite spatial correlations in the presence of activity. To incorporate this in the coarse-grained model, we have introduced the coupling of local order parameters of hot and cold particles with the velocity field describing the local momentum flux due to the density difference of hot and cold species.

The coupling is incorporated by including the leading-order contribution to the free-energy functional, which effectively renormalizes the temperatures of the two species, as introduced in our previous work [28] in analogy with the framework of Model C [3].

The dynamics of the velocity field $u(\boldsymbol{r})$ is governed by the Navier-Stokes equation, with the total stress tensor modeled as $\boldsymbol{\Sigma} = \boldsymbol{\Sigma}_p + \boldsymbol{\Sigma}_a$. $\boldsymbol{\Sigma}_p$ represents the passive contribution arising from density inhomogeneities, as in Model H, while $\boldsymbol{\Sigma}_a$ denotes the active stress associated with the phase separation of the cold and hot species in the mixture. In the phase-separated regime, the cold particles aggregate into dense clusters, surrounded by a dilute background of hot particles, resulting in temperature gradients across the domain interfaces. These interfacial gradients provide a generic mechanism for the effect of activity on the velocity field, wherein phase separation–induced temperature differences are converted into self-generated active stresses through the coupling between compositional inhomogeneities and transport processes. This additional active stress results in enhanced strength and correlation in the velocity field. As a result, the effect of the velocity field remains dynamically significant even at low densities, in contrast to Model H, where hydrodynamic effects are essentially negligible in this limit [42,43].

We include the above inputs to develop the coarse-grained field theory model for the 2-TIPS at low density. The free-energy functionals for cold and hot species are given by

$$\mathcal{F}_{\rm c}[\psi_{\rm c,h}(\boldsymbol{r},t)] = \int \left\{ \frac{\alpha_{\rm c}}{2}\psi_{\rm c}^2 + \frac{\beta_{\rm c}}{4}\psi_{\rm c}^4 + \frac{\kappa_{\rm c}}{2}(\nabla\psi_{\rm c})^2 + \frac{\gamma_{\rm c}}{2}\psi_{\rm c}^2\psi_{\rm h} \right\} d^d r \tag{5}$$

and

$$\mathcal{F}_{\rm h}[\psi_{\rm c,h}(\boldsymbol{r},t)] = \int \left\{ \frac{\alpha_{\rm h}}{2}\psi_{\rm h}^2 + \frac{\beta_{\rm h}}{4}\psi_{\rm h}^4 + \frac{\kappa_{\rm h}}{2}(\nabla\psi_{\rm h})^2 - \frac{\gamma_{\rm h}}{2}\psi_{\rm h}^2\psi_{\rm c} \right\} d^d r, \tag{6}$$

where $d = 2$ is the dimensionality of the system.

In $\mathcal{F}_{\rm c}$ and $\mathcal{F}_{\rm h}$, the first three terms in the integrand describe the self-interaction of each species, and the last two terms are the coupling terms accounting for the interspecies interaction. The coupling terms are motivated by the fact that interspecies interactions effectively reduce the temperature of the hot particles and increase that of the cold particles. The dynamics of $\psi_c(\boldsymbol{r},t)$, $\psi_h(\boldsymbol{r},t)$ are governed by the combined free-energy function $\mathcal{F}_{\rm mix} = \mathcal{F}_{\rm c} + \mathcal{F}_{\rm h}$.

The dynamical equations for the $\psi_c(\boldsymbol{r},t)$, $\psi_h(\boldsymbol{r},t)$, and $\boldsymbol{u}(\boldsymbol{r},t)$ fields are given by

$$\begin{aligned} D_t\psi_{\rm c}(\mathbf{r},t) &= \nabla^2\left(\frac{\delta\mathcal{F}_{\rm mix}}{\delta\psi_{\rm c}}\right) \\ &= \nabla^2\big[\,\alpha_{\rm c}\,\psi_{\rm c} + \beta_{\rm c}\,\psi_{\rm c}^3 - \kappa_{\rm c}\,\nabla^2\psi_{\rm c} \\ &\quad + \gamma_{\rm c}\,\psi_{\rm h}\,\psi_{\rm c} - \tfrac{\gamma_{\rm h}}{2}\,\psi_{\rm h}^2\,\big], \end{aligned} \tag{7}$$

$$\begin{aligned} D_t\psi_{\rm h}(\mathbf{r},t) &= \nabla^2\left(\frac{\delta\mathcal{F}_{\rm mix}}{\delta\psi_{\rm h}}\right) \\ &= \nabla^2\big[\,\alpha_{\rm h}\,\psi_{\rm h} + \beta_{\rm h}\,\psi_{\rm h}^3 - \kappa_{\rm h}\,\nabla^2\psi_{\rm h} \\ &\quad - \gamma_{\rm h}\,\psi_{\rm c}\,\psi_{\rm h} + \tfrac{\gamma_{\rm c}}{2}\,\psi_{\rm c}^2\,\big], \end{aligned} \tag{8}$$

$$\rho D_t\boldsymbol{u} = \eta\nabla^2\boldsymbol{u} - \boldsymbol{\nabla}P + \boldsymbol{\nabla}\cdot(\boldsymbol{\Sigma}_p + \boldsymbol{\Sigma}_a), \tag{9}$$

where $D_t = \partial_t + \gamma(\boldsymbol{u}\cdot\boldsymbol{\nabla})$, and γ is the coupling strength. In Eq. (9), the first term on the right-hand side represents shear viscosity with coefficient η and the second term represents the contribution from pressure gradient. The passive component of the stress tensor gives $\boldsymbol{\nabla}\cdot\boldsymbol{\Sigma}_p = -(\psi_h\boldsymbol{\nabla}\mu_h + \psi_c\boldsymbol{\nabla}\mu_c)$, where $\mu_c = \frac{\delta\mathcal{F}_{\rm mix}}{\delta\psi_{\rm c}}$ and $\mu_h = \frac{\delta\mathcal{F}_{\rm mix}}{\delta\psi_{\rm h}}$ are the chemical potential for the cold and hot species, respectively. The active component of stress is given by $\boldsymbol{\Sigma}_a = \chi_{cg}[(\partial_i\phi)(\partial_j\phi) - \frac{1}{2}\delta_{ij}(\nabla\phi)^2]$, where $\phi(\boldsymbol{r},t) = \psi_h(\boldsymbol{r},t) - \psi_c(\boldsymbol{r},t)$ describes the local phase separation order parameter between the cold and hot species. The coefficient χ_{cg} is the activity in the CG model and is defined as $\chi_{cg} = \alpha_h - \alpha_c$, which is a measure of the relative temperature difference between two species. It is important to note that the form of active stress and the results are unaffected under $\phi \to -\phi$ transformation. The active stress quantifies the excess interfacial stress generated by the temperature gradient between the interior of the cold domains and the surrounding hot medium for a phase separating droplet.

The coarse-grained model is simulated in a two-dimensional square box of size L with periodic boundary conditions along both directions. Equations (7), (8), and (9) are simulated using a finite time central space (FTCS) integration scheme with spatial and temporal grid size ΔX and Δt, respectively, satisfying the criteria $\frac{\Delta t}{(\Delta X)^2} < \frac{1}{2}$ for numerical stability. To solve Eq. (9) within the discretization scheme, we have used the stream function method [44]. In our simulation, we set $\Delta X = 1.0$ and $\Delta t = 0.01$.

The average value of the density order parameter for the cold and hot species can be defined as $\psi_{0,c/h} = \frac{1}{L^2}\sum_{\boldsymbol{r}} \psi_{c/h}(\boldsymbol{r})$. The mean density of the cold and hot species can be approximately calculated as $\rho_{0,c/h} \approx \frac{1+\psi_{0,c/h}}{2}$. The mean density of the system, ρ_0, is given by $\rho_0 = \rho_{0,c} + \rho_{0,h}$. $\psi_{0,c/h} \approx 0$ represents a densely packed system of cold and hot particles, with $\psi_{0,c/h} < 0$ indicating a decrease in overall density. The mixture is symmetric when $\psi_{0,c} = \psi_{0,h}$ and asymmetric otherwise. Initially, at each lattice point, $\psi_{c/h}$ are distributed uniformly in the interval $[-\xi, \xi]$ around $\psi_{0,c/h}$, where $\xi = 0.05$, and the velocity field $\boldsymbol{u}(\boldsymbol{r}) \equiv (u_x(\boldsymbol{r}), u_y(\boldsymbol{r}))$ is distributed randomly at each lattice point. The results presented in this article correspond to system size $L = 1024$, for which the system is simulated for 10^6 time steps. One simulation step is counted when the state of the system (i.e., $\{\psi_c, \psi_h, \boldsymbol{u}\}$) is updated once. For better statistics, data (except snapshots) are averaged over 100 independent realizations.

In our simulations, we keep hot and cold particles in equal proportions in the mixture, i.e., $\psi_{0,c} = \psi_{0,h} = \psi_0$. In this study, we focus in the extreme low-density regime by fixing $\psi_0 \in [-0.60, -0.70]$, which corresponds to the average density of cold and hot species in the range $\rho_{0,c/h} \in [0.15, 0.20]$. The total density of the system is given by $\rho_0 = \rho_{0,c} + \rho_{0,h}$.

B. Results

In Fig. 6(a), the time evolution of the mixture starting from a homogeneously mixed state is described through a series of snapshots of the ϕ -field. Starting from the homogeneous state, it takes some time before the domains of the cold particles ($\phi < 0$) emerge as small droplets through nucleation (see Movie 3 [50]). Once the droplets appear, the size of the droplets grows rapidly with time mainly through coalescence (see Movie 4 [50]).

To characterize the growth of the droplets with time, we calculated the spatial two-point correlation function $C_\phi(r, t)$ as defined in Eq. (2). The plot of $C_\phi(r, t)$ versus r at different times is shown in the inset of Figs. 6(b)–6(d) for three different activities. The slower decay of the correlation at successive times implies the growth of domains. The characteristic length, denoted by $l(t)$, is calculated as the 0.5 crossing of the $C_\phi(r, t)$. The curve of $C_\phi(r)$ at different times collapses on a single master curve when plotted against the scaled distance $r/l(t)$ as shown in the main plot window of Figs. 6(b)–6(d). This implies the existence of a scaling regime where the domain morphology is statistically independent of time and differs in the characteristic length scale $l(t)$ only. In the scaling regime, domain growth follows a power-law scaling $l(t) \sim t^{1/z}$ with an exponent $1/z$. In our system, we found $\frac{1}{z} \approx 0.70$ independent of density in range $\rho_0 \in [0.30, 0.45]$, as shown in Fig. 6(e). We also observed that the growth exponent is independent of activity for the density in the given range, as shown in Fig. 6(f). Thus, the growth law obtained from the CG model is consistent with that obtained from the MD simulations (Fig. 3). The enhanced growth kinetics in 2-TIPS is solely due to this active stress, and we compared the results for with and without active stress and found that the growth exponent is much smaller when the active stress Σ_a is turned off as shown in Fig. 9 in Appendix C.

In the scaling regime, domain growth proceeds primarily through droplet coalescence. We find that smaller droplets exhibit translational motion (see Movie 5 [50]), while larger droplets remain nearly immobile (see Movie 4 [50]). To characterize the dynamics of the smaller droplets, we calculate the MSD of the center of mass of the droplets, $\Delta(t)$. As shown in Fig. 6(g), $\Delta(t)$ varies as $\sim t^2$, which implies ballistic dynamics of the smaller droplets.

IV. CONCLUSION

In this study, we have examined the phase separation kinetics of 2-TIPS in the low-density regime using molecular dynamics (MD) simulations, and we developed a corresponding coarse-grained (CG) model to capture the system's behavior at mesoscopic scales. The CG model couples the density order parameter fields to a velocity field that accounts for the local momentum flux arising from both hot and cold species. Following the quench, as the cold particles begin to form domains, the resulting temperature contrast across domain boundaries generates an additional interfacial stress, whose magnitude scales with the temperature difference—i.e., the activity between the two species.

At low density, the hot and cold species phase separation proceeds via the nucleation of cold clusters embedded in a hot majority phase, whereas the same system at high density phase separates through the spinodal decomposition [28]. After nucleation, these clusters undergo ballistic motion and grow through coalescence, leading to rapid coarsening. Our study shows that the domain size grows as $\approx t^{0.70}$ in both MD and CG methods. Furthermore, the growth exponent obtained from our study shows excellent agreement with the prediction from ballistic aggregation theory. The phase separation kinetics we found in our MD as well as CG simulations is very different from the 2-TIPS using stochastic Langevin dynamics [13]. The separation kinetics depends strongly on microscopic dynamics and thermostat choice. In overdamped systems, cluster motion is diffusive with a growth exponent of 1/4 [13], whereas our Nosé-Hoover approach accesses an inertial regime with ballistic cluster motion and faster coarsening. Unlike Langevin dynamics, which suppress inertia, our model captures momentum transport consistent with a Navier-Stokes-like description. This highlights the key role of inertia in determining 2-TIPS kinetics.

In the present 2-TIPS system, the temperature difference is local rather than global, unlike scenarios where pure ballistic growth is expected. While ballistic aggregation typically yields faster coarsening, the exponent observed here is lower, reflecting the interplay between local driving and interactions. This indicates that, although clusters exhibit ballistic dynamics locally, the growth mechanism differs from ideal ballistic coarsening due to spatially heterogeneous temperature fields. Also the phase separation observed here is significantly different from that of EBMs in the dilute limit wherein the system reaches a metastable state and does not phase separate spontaneously.

These results reveal a distinct kinetic regime from equilibrium mixtures and highlight the universal relevance of coalescence [39,45], a process central to phenomena ranging from planet formation [10,46] and raindrop growth [47] to colloidal aggregation [48,49].

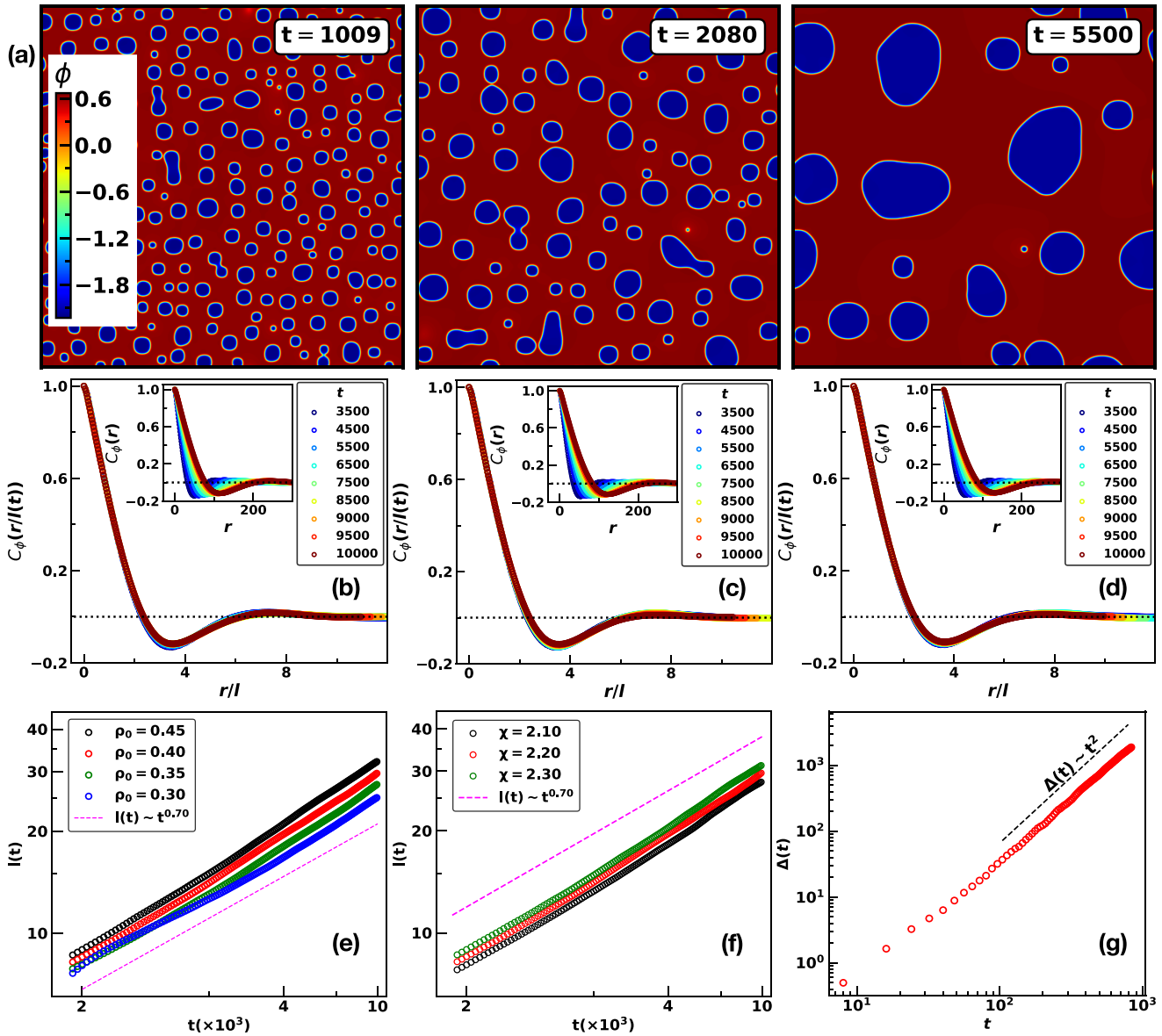

FIG. 6. Panel (a) shows the domain growth in the mixture through a series of snapshots at different times, where the color shows the value of the phase separation order parameter ϕ according to the colorbar. Panels (b)–(d) show the plots of scaled correlation $C(r/l)$ vs r/l at different times for three different values of activity χ at a fixed density $\rho_0 \approx 0.40$: (b) $\chi = 2.10$, (c) $\chi = 2.20$, and (d) $\chi = 2.30$. In each scale, the plot of unscaled correlation functions $C(r)$ vs r at different times is shown in the corresponding inset plot. Panel (e) shows the plot of time-dependent characteristics length $l(t)$ vs t on a log-log scale for different densities ρ_0 at a fixed activity $\chi_{cg} = 2.20$. Panel (f) shows the $l(t)$ vs t plot on a log-log scale for different activities χ at a fixed density $\rho_0 \approx 0.40$. Panel (g) shows the plot of MSD of the center of droplets, $\Delta(t)$ vs t, in the scaling regime. Time $t = 0$ in the plot is the reference time after which a droplet is tracked. Parameters: system size $L = 1024$.

The nonequilibrium phase separation kinetics in 2-TIPS is rich, showing nontrivial dependence on density. In the future, we would further extend our study of kinetics to include hot and cold spherocylinders to see the influence of shape anisotropy on phase separation kinetics.

ACKNOWLEDGMENTS

P.K.M. and N.V. gratefully acknowledge an IRHPA grant from SERB (now ANRF) (No. IPA/2020/000034). P.K.M thanks ANRF, India, for support through the JC Bose Grant (ANRF/JBG/2025/000227/PS). P.S.M. thanks UGC for the research fellowship. S.M. thanks DST, SERB (INDIA), Projects No. CRG/2021/006945 and No. MTR/2021/000438, for financial support.

DATA AVAILABILITY

The data that support the findings of this article are not publicly available. The data are available from the authors upon reasonable request.

APPENDIX A: ADDITIONAL MD RESULTS FOR SYSTEM SIZE $N = 100\,000$ PARTICLES

In Fig. 7, we present the MD results for $N = 100\,000$.

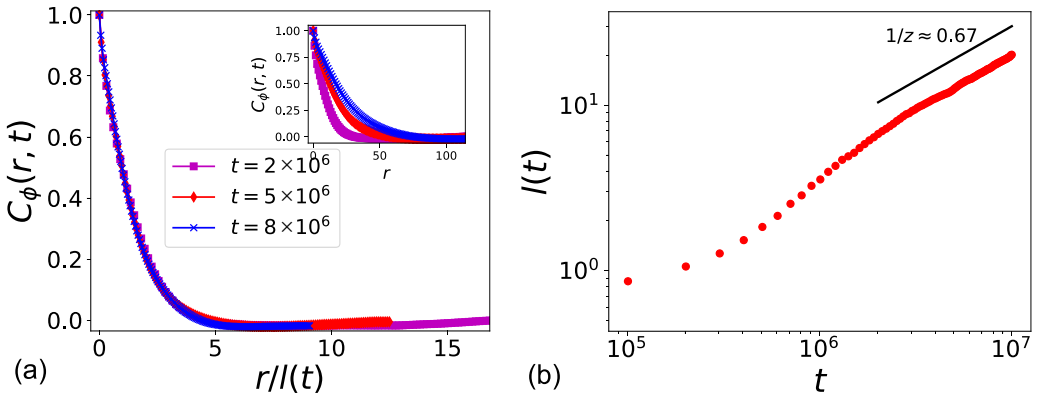

FIG. 7. MD results for system size $N = 100\,000$. (a) Plot of the spatial correlation function $C_\phi(r,t)$ as a function of rescaled distance $r/l(t)$, at density $\rho^* = 0.1$ for $T_h^* = 25$, at different instants of time. The $C_\phi(r,t)$ at different times collapses onto a single master plot demonstrating dynamic scaling. The inset illustrates a plot of spatial correlation function $C_\phi(r,t)$ as a function of distance between the points r at density $\rho^* = 0.1$ for $T_h^* = 25$ at different instants of time. (b) Log-log plot of characteristic length $l(t)$ vs time t for $T_h^* = 25$ show algebraic growth of $l(t)$. The value of growth exponent $1/z$ at late times is equal to 0.67 ± 0.03 for $T_h^* = 25$. The results were obtained by averaging over five independent realizations.

APPENDIX B: AVERAGE MASS OF 20 LARGEST CLUSTERS WITH TIME

Figure 8 illustrates the growth of the 20 largest cold clusters with time.

APPENDIX C: RESULTS WITHOUT ACTIVE STRESS

In Fig. 9(a) we show the results of growth kinetics with ($\Sigma_a \neq 0$) and without active stress ($\Sigma_a = 0$) in Eq. (9). It is evident that, in the absence of active stress, the growth exponent is much smaller than 0.70 [Fig. 9(a)]. Further, we also observe that the mechanism of domain coarsening in the case without active stress is predominantly Ostwald ripening, unlike the system with active stress. This emphasizes that the active stress emerging from the temperature gradient between the interior and the exterior of the domains is an essential component for understanding the faster domain growth in the system. Additionally, in Fig. 9(b) we also show the scaling of the two-point correlation function $C(r)$ at different times for $\Sigma_a = 0$.

APPENDIX D: DESCRIPTION OF THE MOVIES

Movie 1: Kinetics of phase separation in 2-TIPS at low density from MD simulations [50]. This movie depicts the phase separation kinetics in 2-TIPS at low density, in a symmetric binary mixture of hot (red) and cold (blue) particles. After the quench, cold nuclei nucleate within a sea of hot particles. These cold clusters then migrate and merge with others, progressively forming larger phase-separated structures. The ballistic motion of the clusters toward one another indicates an effective attractive interaction driving the coalescence process. Parameters: System size $N = 80\,000$, quench temperature $T_h^* = 25$, density $\rho^* = 0.1$.

Movie 2: Ballistic motion of a few cold clusters from MD simulation [50]. This movie provides a magnified view of Movie 1, wherein the ballistic migration of cold clusters toward each other becomes evident. Parameters: System size $N = 80\,000$, quench temperature $T_h^* = 25$, density $\rho^* = 0.1$.

Movie 3: Emergence of phase separation in the coarse-grained model [50]. This movie shows the emergence

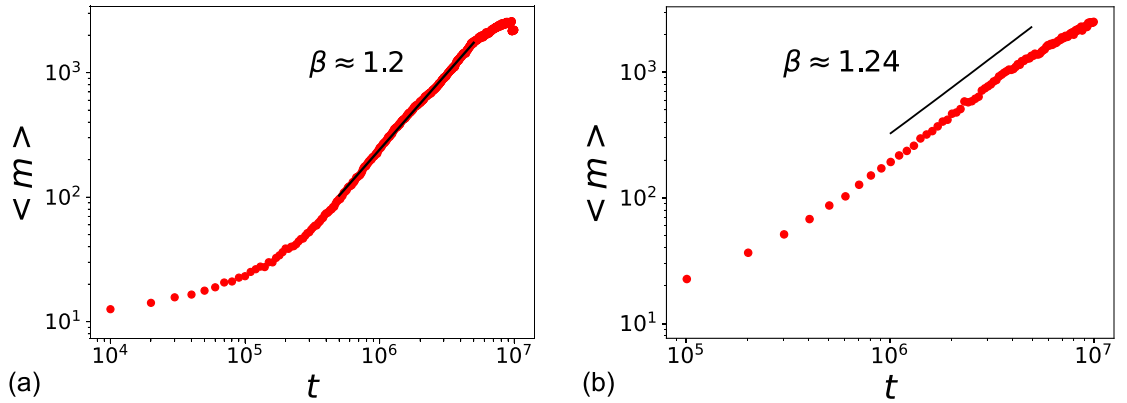

FIG. 8. Growth of 20 largest cold clusters with time. Panels (a) and (b) depict plots of average mass of 20 largest clusters $\langle m \rangle$ vs time for $T_h^* = 25$ and 40, respectively. The associated mass growth exponent ($m \sim t^\beta$) is $\beta = 1.16$ and 1.24 for the same temperatures. These values are in close agreement with the predictions of ballistic agglomeration theory.

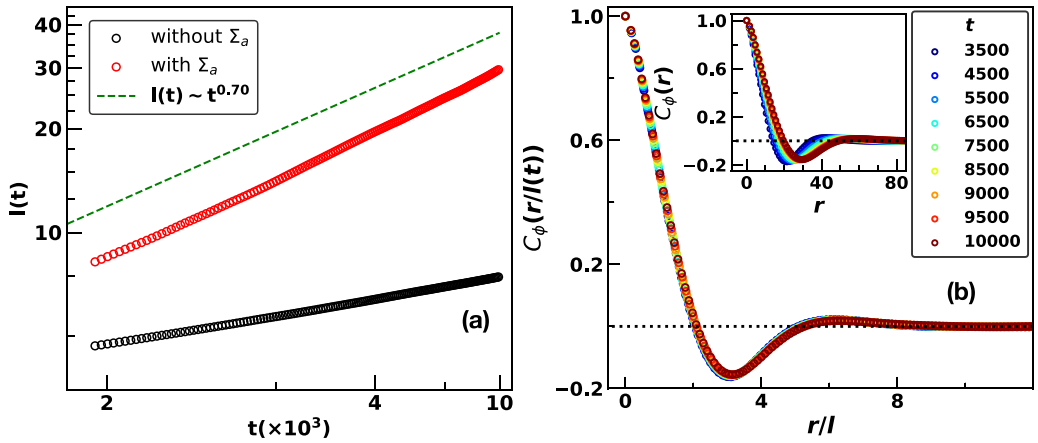

FIG. 9. Panel (a) compares the plot of $l(t)$ vs t with and without active stress term Σ_a for density $\rho_0 = 0.40$ and activity $\chi = 2.20$. Panel (b) shows the scaling of the collapse of the scaled correlation function $C[r/l(t)]$ vs r/l at different times without active stress Σ_a for the same set of parameters as in panel (a). The rest of the parameters are the same as in Fig. 6.

of phase separation between cold and hot particles in the mixture starting from a homogeneously mixed state. The heatmap depicts the local phase separation order parameter, defined as $\phi(\boldsymbol{r}, t) = \psi_h(\boldsymbol{r}, t) - \psi_c(\boldsymbol{r}, t)$, with the corresponding values indicated by the colorbar. Regions where $\phi < 0$ ($\phi > 0$) correspond to the cold (hot) majority domains. The movie clearly shows the emergence of cold droplets through nucleation events. Parameters: System size $L = 512$, activity $\chi = 2.20$, off-criticality $\psi_0 = -0.60$ ($\rho_0 = 0.40$).

Movie 4: Droplet coalescence in the coarse-grained model [50]. This movie illustrates the coarsening dynamics of the ϕ field via droplet coalescence, focusing on a subregion of the entire simulation box. The movie clearly shows that the small droplet shows significant translational dynamics, whereas larger droplets remain largely immobile while exhibiting shape modulations either due to dynamics of larger droplets in its vicinity or before the coalescence events. The details of the heatmap are the same as in Movie 3. Parameters: System size $L = 512$ (zoomed into a 250×250 box in the system), activity $\chi = 2.20$, off-criticality $\psi_0 = -0.60$ ($\rho_0 = 0.40$).

Movie 5: Droplet dynamics in the coarse-grained model [50]. This movie highlights the droplet dynamics by focusing on a single droplet within the system. The details of the heatmap are the same as in Movie 3. Parameters: System size $L = 512$, activity $\chi = 2.20$, off-criticality $\psi_0 = -0.60$ ($\rho_0 = 0.40$).

[1] S. Puri, Kinetics of phase transitions, in *Kinetics of Phase Transitions* (CRC Press, Boca Raton, 2009), pp. 13–74.

[2] A. J. Bray, Theory of phase-ordering kinetics, Adv. Phys. **43**, 357 (1994).

[3] P. C. Hohenberg and B. I. Halperin, Theory of dynamic critical phenomena, Rev. Mod. Phys. **49**, 435 (1977).

[4] M. E. Cates and E. Tjhung, Theories of binary fluid mixtures: From phase-separation kinetics to active emulsions, J. Fluid Mech. **836**, P1 (2018).

[5] D. A. Porter, K. E. Easterling, and M. Y. Sherif, *Phase Transformations in Metals and Alloys*, 3rd ed. (CRC Press, Boca Raton, 2009).

[6] M. C. Marchetti, J.-F. Joanny, S. Ramaswamy, T. B. Liverpool, J. Prost, M. Rao, and R. A. Simha, Hydrodynamics of soft active matter, Rev. Mod. Phys. **85**, 1143 (2013).

[7] P. Romanczuk, M. Bär, W. Ebeling, B. Lindner, and L. Schimansky-Geier, Active Brownian particles, Eur. Phys. J. Spec. Top. **202**, 1 (2012).

[8] J. Toner, Y. Tu, and S. Ramaswamy, Hydrodynamics and phases of flocks, Ann. Phys. (NY) **318**, 170 (2005).

[9] S. Ramaswamy, Active fluids, Nat. Rev. Phys. **1**, 640 (2019).

[10] A. Johansen and M. Lambrechts, Forming planets via pebble accretion, Annu. Rev. Earth Planet Sci. **45**, 359 (2017).

[11] T. Vicsek and A. Zafeiris, Collective motion, Phys. Rep. **517**, 71 (2012).

[12] H. H. Wensink, J. Dunkel, S. Heidenreich, K. Drescher, R. E. Goldstein, H. Löwen, and J. M. Yeomans, Meso-scale turbulence in living fluids, Proc. Natl. Acad. Sci. USA **109**, 14308 (2012).

[13] S. N. Weber, C. A. Weber, and E. Frey, Binary mixtures of particles with different diffusivities demix, Phys. Rev. Lett. **116**, 058301 (2016).

[14] S. S. N. Chari, C. Dasgupta, and P. K. Maiti, Scalar activity induced phase separation and liquid–solid transition in a Lennard-Jones system, Soft Matter **15**, 7275 (2019).

[15] N. Ganai, S. Sengupta, and G. I. Menon, Chromosome positioning from activity-based segregation, Nucl. Acids Res. **42**, 4145 (2014).

[16] C.-P. Li, H.-B. Chen, and Z.-G. Zheng, Double-temperature ratchet model and current reversal of coupled Brownian motors, Front. Phys. **12**, 120507 (2017).

[17] M. Xu, J. L. Ross, L. Valdez, and A. Sen, Direct single molecule imaging of enhanced enzyme diffusion, Phys. Rev. Lett. **123**, 128101 (2019).

[18] E. McCarthy, R. K. Manna, O. Damavandi, and M. L. Manning, Demixing in binary mixtures with differential diffusivity at high density, Phys. Rev. Lett. **132**, 098301 (2024).
[19] A. Al-Hiyasat, S. Ro, and J. Tailleur, Statistical mechanics of a cold tracer in a hot bath, Phys. Rev. E **113**, 034127 (2026).
[20] N. Venkatareddy, S.-T. Lin, and P. K. Maiti, Phase behavior of active and passive dumbbells, Phys. Rev. E **107**, 034607 (2023).
[21] J. Chattopadhyay, S. Ramaswamy, C. Dasgupta, and P. K. Maiti, Two-temperature activity induces liquid-crystal phases inaccessible in equilibrium, Phys. Rev. E **107**, 024701 (2023).
[22] N. Venkatareddy, J. Mandal, and P. K. Maiti, Effect of confinement and topology: 2-TIPS vs. MIPS, Soft Matter **19**, 8561 (2023).
[23] J. Chattopadhyay, S. Pannir-Sivajothi, K. Varma, S. Ramaswamy, C. Dasgupta, and P. K. Maiti, Heating leads to liquid-crystal and crystalline order in a two-temperature active fluid of rods, Phys. Rev. E **104**, 054610 (2021).
[24] J. Chattopadhyay, J. Mandal, and P. K. Maiti, Stability of the chiral crystal phase and breakdown of the cholesteric phase in mixtures of active–passive chiral rods, Soft Matter **20**, 2464 (2024).
[25] A. Y. Grosberg and J.-F. Joanny, Dissipation in a system driven by two different thermostats, Polym. Sci. Ser. C **60**, 118 (2018).
[26] A. Y. Grosberg and J.-F. Joanny, Nonequilibrium statistical mechanics of mixtures of particles in contact with different thermostats, Phys. Rev. E **92**, 032118 (2015).
[27] E. Ilker and J.-F. Joanny, Phase separation and nucleation in mixtures of particles with different temperatures, Phys. Rev. Res. **2**, 023200 (2020).
[28] N. Venkatareddy, P. S. Mondal, J. Mandal, S. Mishra, and P. K. Maiti, Growth laws and universality in two-temperature induced phase separation: Microscopic and coarse-grained approach, Phys. Rev. E **112**, 015409 (2025).
[29] I. Lifshitz and V. Slyozov, The kinetics of precipitation from supersaturated solid solutions, J. Phys. Chem. Solids **19**, 35 (1961).
[30] H. Tanaka, Viscoelastic phase separation, J. Phys.: Condens. Matter **12**, R207 (2000).
[31] Y. Fily, S. Henkes, and M. C. Marchetti, Freezing and phase separation of self-propelled disks, Soft Matter **10**, 2132 (2014).
[32] S. Pattanayak, S. Mishra, and S. Puri, Ordering kinetics in the active Model B, Phys. Rev. E **104**, 014606 (2021).
[33] A. P. Thompson, H. M. Aktulga, R. Berger, D. S. Bolintineanu, W. M. Brown, P. S. Crozier, P. J. in 't Veld, A. Kohlmeyer, S. G. Moore, T. D. Nguyen, R. Shan, M. J. Stevens, J. Tranchida, C. Trott, and S. J. Plimpton, LAMMPS - a flexible simulation tool for particle-based materials modeling at the atomic, meso, and continuum scales, Comput. Phys. Commun. **271**, 108171 (2022).
[34] D. J. Evans and B. L. Holian, The Nose–Hoover thermostat, J. Chem. Phys. **83**, 4069 (1985).
[35] K. Binder, S. Puri, S. K. Das, and J. Horbach, Phase separation in confined geometries, J. Stat. Phys. **138**, 51 (2010).
[36] S. Roy and S. K. Das, Nucleation and growth of droplets in vapor-liquid transitions, Phys. Rev. E **85**, 050602(R) (2012).
[37] J. Midya and S. K. Das, Kinetics of vapor-solid phase transitions: Structure, growth, and mechanism, Phys. Rev. Lett. **118**, 165701 (2017).
[38] K. Khan, S. U. Rehman, K. Aziz, S. Fong, and S. Sarasvady, DBSCAN: Past, present and future, in *Proceedings of the Fifth International Conference on the Applications of Digital Information and Web Technologies (ICADIWT 2014)* (IEEE, Bangalore, India, 2014), pp. 232–238.
[39] P. L. Krapivsky, S. Redner, and E. Ben-Naim, *A Kinetic View of Statistical Physics* (Cambridge University Press, Cambridge, 2010).
[40] S. Paul and S. K. Das, Ballistic aggregation in systems of inelastic particles: Cluster growth, structure, and aging, Phys. Rev. E **96**, 012105 (2017).
[41] S. Paul, A. Bera, and S. K. Das, How do clusters in phase-separating active matter systems grow? A study for vicsek activity in systems undergoing vapor–solid transition, Soft Matter **17**, 645 (2021).
[42] H. Tanaka, Hydrodynamic interface quench effects on spinodal decomposition for symmetric binary fluid mixtures, Phys. Rev. E **51**, 1313 (1995).
[43] R. Shimizu and H. Tanaka, A novel coarsening mechanism of droplets in immiscible fluid mixtures, Nat. Commun. **6**, 7407 (2015).
[44] C. Pozrikidis and J. H. Ferziger, *Introduction to Theoretical and Computational Fluid Dynamics* (Oxford University Press, New York, USA, 1997).
[45] F. Leyvraz, Scaling theory and exactly solved models in the kinetics of irreversible aggregation, Phys. Rep. **383**, 95 (2003).
[46] V. S. Safronov, *Evolution of the Protoplanetary Cloud and Formation of the Earth and the Planets* (NASA Tech Translations, Washington, DC, USA, 1972).
[47] H. R. Pruppacher and J. D. Klett, *Microphysics of Clouds and Precipitation* (Springer, Dordrecht, Netherlands, 1997).
[48] M. Lin, H. Lindsay, D. Weitz, R. Ball, R. Klein, and P. Meakin, Universality in colloid aggregation, Nature (London) **339**, 360 (1989).
[49] C. P. Royall, M. A. Faers, S. L. Fussell, and J. E. Hallett, Real space analysis of colloidal gels: Triumphs, challenges and future directions, J. Phys.: Condens. Matter **33**, 453002 (2021).
[50] N. Venkatareddy, P. S. Mondal, S. Mishra, and P. K. Maiti, Supplementary Movies for "Phase separation kinetics of two-temperature induced phase separation at low density: Cluster growth by ballistic agglomeration" [Video recording], Zenodo, 2026, https://doi.org/10.5281/zenodo.21966101